Sulfated Well-Defined Mesoporous Nanostructured Zirconia for Levulinic Acid Esterification

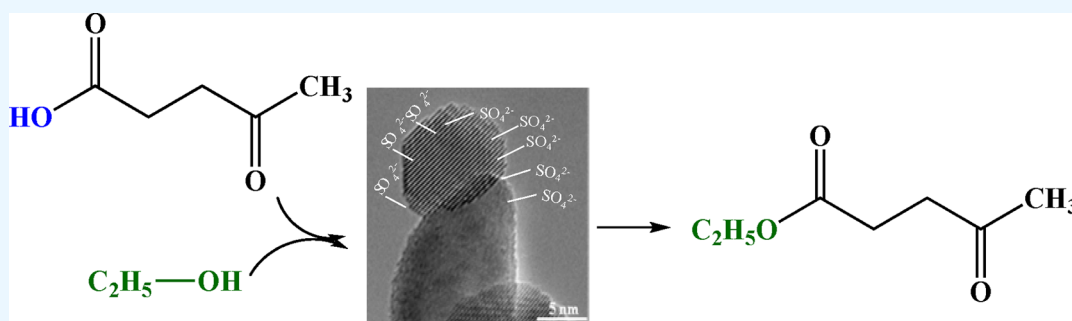Salaheddine Lanaya, Yousra El Jemli, Khadija Khallouk, Karima Abdelouahdi, Abdellah Hannioui, Abderrahim Solhy, and Abdellatif Barakat*

ACCESS | Metrics & More | Article Recommendations | Supporting Information

ABSTRACT: Well-organized zirconia (ZrO_2) nanoparticles forming mesoporous materials have been successfully synthesized via a facile micelle-templating method using cetyltrimethylammonium bromide as a structure-directing template to control the nucleation/growth process and porosity. The systematic use of such a surfactant in combination with a microwave-assisted solvothermal (cyclohexane/water) reaction enabled the control of pore size in a narrow-size distribution range (3−17 nm). The effect of solvent mixture ratio on the porosity of the synthesized oxide was determined, and the controlled growth of zirconia nanoparticles was confirmed by means of powder X-ray diffraction, small-angle X-ray scattering, transmission electron microscopy, selected area electron diffraction, high-resolution transmission electron microscopy, X-ray photoelectron spectroscopy, thermogravimetric analysis, and Fourier transform infrared spectroscopy as well as N_2 physisorption isotherm analysis. Then, the as-prepared nanostructured zirconia oxides were treated with sulfuric acid to have sulfated samples. The catalytic performances of these mesoporous zirconia nanoparticles and their sulfated samples were tested for levulinic acid (LA) esterification by ethanol, with quantitative conversions of LA to ethyl levulinate after 8 h of reaction.

1. INTRODUCTION

Zirconia is an important class of advanced oxide.[1] This material has been widely studied because of its unique properties such as hardness, chemical stability, refraction, and ionic conductivity.[1] These distinctive properties make zirconia a good choice for a wide range of applications, such as solid fuel cells, ceramics, thermal barrier coating materials, catalysts, pigments, and luminescent materials or sensors when doped by rare earth elements.[2−18] These applications depend not only on the structural properties and crystallinity, particle size, and morphologies of zirconia but also on its porosity.[19] Zirconia has been synthesized by various methods such as sol−gel process,[20−22] coprecipitation[23,24] hydrothermal or solvothermal synthesis,[25−28] pulsed plasma technique,[29] aerosol pyrolysis,[30,31] and more recently, sustainable methods such as gelation of alginate,[32] precipitation by hydroxypropyl-β-cyclodextrin,[33] use of lysozyme, which is a cationic antibacterial enzyme,[34] and use of *Fusarium oxysporum*, which is a species of plant parasitic fungus.[35] The synthesis of mesoporous zirconia with narrow pore size distribution for specific applications has received ample attention.[36−40] Pârvulescu et al. prepared mesoporous zirconia via a sol−gel procedure using ammonium salts as surfactants with linear alkyl chains wherein the effects of various parameters on the porous texture, especially ratios of the Zr/H_2O and $Zr/$ surfactant, were examined to establish their influence on the porous texture (surface area and pore size).[41] Similarly, Jean-Luc Blin et al. adopted a sol−gel mineralization route using nonionic alkyl-PEO surfactants followed by a hydrothermal treatment leading to mesoporous zirconia with a macroporous hierarchical funnel-like structure.[42] Recently, the synthesis of nanocrystalline mesoporous tetragonal zirconia having a high surface area (193.1 m^2/g) was reported via a precipitation

method followed by hydrothermal treatment using ethylenediamine as a precipitating agent and zirconyl chloride as a precursor of zirconium.[43] Subsequent work focused on the elaboration of the sulfated zirconium oxide with organized mesoporous channels for potential applications in heterogeneous catalysis.[44−46] The use of pore formers and stabilizers to maintain mesopores during heat treatment has also been studied.[47,48]

The use of microwave (MW) heating in the synthesis of inorganic materials is a promising strategy because of its rapid and uniform heating and short reaction time.[49,50] Numerous studies have described the MW-assisted synthesis of zirconia, as exemplified by the synthesis of nanostructured tetragonal zirconia via the sol−gel route using citric acid as a structuring agent.[51] Similarly, nanocrystalline zirconia was synthesized by hydrothermal-assisted MW heating using only zirconium(IV) tetrachloride and sodium hydroxide as reagents.[52] When the reactions were carried out at temperatures between 150 and 200 °C and at a pH of 7, this method yielded tetragonal phase only. Beyond 200 °C, at that pH, it produced a mixture of tetragonal and monoclinic phases but with a predominance of the tetragonal phase. Under very acidic or basic mediums, it yielded mixtures of these two phases, independent of the reaction temperature.

Levulinic esters are promising biobased building blocks which could replace petroleum derivatives potentially usable in the pharmaceutical and food industry as well as potential alternative solvents.[53] These esters are obtained from the esterification of levulinic acid in the presence of an alcohol by the action of a Brönsted acid catalyst, typically homogeneous acid catalysts such as sulfuric acid[54] and hydrochloric acid[55] or heterogeneous catalysts such as sulfated metal oxides,[56,57] sulfated zirconosilicates,[58] zeolites,[59−63] MOFs,[64] zirconia supported on silica SBA-15,[65] dodecatungstophosphoric acid supported on montmorillonite K10,[66,14] Well−Dawson heteropolyacid on silica,[67] and Keggin acid on silica.[68] Yadav et al.[69] used a chlorosulfonic acid sulfated zirconia to have a more stable, strongly acidic, and more active catalyst than a sulfuric acid modified zirconia, according to their conclusions. This sulfated zirconia has made it possible to obtain numerous levulinic esters by testing several alcohols with yields greater than 90%. In another study, Kuwahara and co-workers developed a catalyst through the incorporation of silicon in sulfated zirconia, which made it possible to obtain catalytic materials of varied structure and acidity, with respect to this reaction.[70] Su et al.[71] developed a functionalized zirconia with organosilicate benzene bridges and a heteropolyacid. They concluded that there was an interaction between the support (zirconia) and the Keggin structure of the heteropolyacid because of the Brönsted acidity of the zirconia. This interaction had the effect of obtaining a higher acidity than heteropolyacid alone, while benefiting from the mesoporous volume of zirconia allowing a homogeneous dispersion. In another study, the same authors succeeded in developing catalytic materials of the same type with a mesoporosity and a large specific surface, which significantly increased the acid sites.[72] The meso-structuring organization of the catalytic materials further facilitates mass transfer and thus promotes accessibility to acid sites to obtain maximum yield of levulinic esters.[73] Therefore, recent work emphasizes the calibrated mesoporosity of catalytic materials and the acid sites rates in order to have increased performance for this reaction.[74]

Building upon the initial success in the hierarchical self-assembly of nanomaterials under sustainable conditions,[32] we have developed a facile route to prepare mesoporous nanostructured zirconia with good control over porosity and morphology. The effects of additive, urea, and cetyltrimethylammonium bromide (CTAB) concentration and the solvent ratio deployed under MW conditions are reported here. Moreover, catalytic tests of the esterification of levulinic acid with ethanol to have ethyl levulinate in the presence of functionalized zirconia samples by sulfate groups were carried out. The influence of zirconia porosity on the catalytic activity of the reaction conversion was discussed.

2. EXPERIMENTAL METHODS

2.1. Materials. Cetyltrimethylammonium bromide, zirconium butoxide, cyclohexane, urea, sulfuric acid, levulinic acid, and ethanol were purchased from Sigma-Aldrich and used without further purification. The sample heating was performed with a microwave oven from Strat-Synth (Milestone S.r.l.) in a Sorvall WX Ultra Series centrifuge from Thermo Scientific. A thermostatic vacuum dryer (Vacuo-Temp) was used for drying materials.

2.2. Synthesis of Mesoporous Nanostructured Zirconia. In a typical synthesis, two solutions, designated S1 and S2, were prepared. For S1, zirconium butoxide was dissolved in a volume of cyclohexane varying from 10 to 50 mL at room temperature under stirring for 20 min. For S2, 1.00 g of CTAB and 0.6 g of urea were dissolved in 10 to 50 mL water at room temperature, and the solution was stirred for 30 min. Then, S2 was slowly added to S1, and the mixture was stirred at room temperature for 1 h. The resulting milky solution was then transferred to a Teflon-sealed MW reactor and was exposed to MW irradiation (400 W) at 120 °C for 30 min. After it was cooled to room temperature, the mixture was centrifuged, and the precipitate was washed thoroughly with distilled water and ethanol to remove any residual surfactant. Six samples of dried ZrO_2 were prepared with varying cyclohexane/water volume ratios (mL/mL): 50/10, 40/20, 30/30, 20/40, 10/50, and 0/60, which were termed Zir-5/1-D, Zir-4/2-D, Zir-3/3-D, Zir-2/4-D, Zir-1/5-D, and Zir-0/6-D, respectively. These samples were then vacuum-dried at 80 °C and calcined at 500 °C for 4 h in air. The calcined samples were designated Zir-5/1-C, Zir-4/2-C, Zir-3/3-C, Zir-2/4-C, Zir-1/5-C, and Zir-0/6-C, respectively.

2.3. Functionalization of Mesoporous Zirconia Samples by $SO_4^{2−}$ Groups. A mass of each calcined mesoporous zirconia sample as-prepared (1g) was introduced into 15 mL of a sulfuric acid solution (0.1 M). The mixture was stirred at room temperature for 2 h. The samples were then filtered, dried in an oven at 80 °C for 12 h, and then calcined at 500 °C for 2 h under air. The sulfated mesoporous zirconia samples were denoted: Zir-5/1-C@$SO_4^{2−}$ (Catal. 1), Zir-4/2-C@$SO_4^{2−}$ (Catal. 2), Zir-3/3-C@$SO_4^{2−}$ (Catal. 3), Zir-2/4-C@$SO_4^{2−}$ (Catal. 4), Zir-1/5-C@$SO_4^{2−}$ (Catal. 5), and Zir-0/6-C@$SO_4^{2−}$ (Catal. 6), respectively.

2.4. Characterization. Thermogravimetric analysis (TGA) was conducted under air in a TA Instrument Q500 with a 10 °C/min ramp between 25 and 1000 °C. Fourier transform infrared (FTIR) spectra of samples embedded in KBr pellets were measured on a Bruker Vector 22 spectrometer. X-ray diffraction (XRD) patterns were obtained at room temperature on a Bruker AXS D-8 diffractometer using Cu Kα radiation in Bragg−Brentano geometry (q-2q). Transmission electron
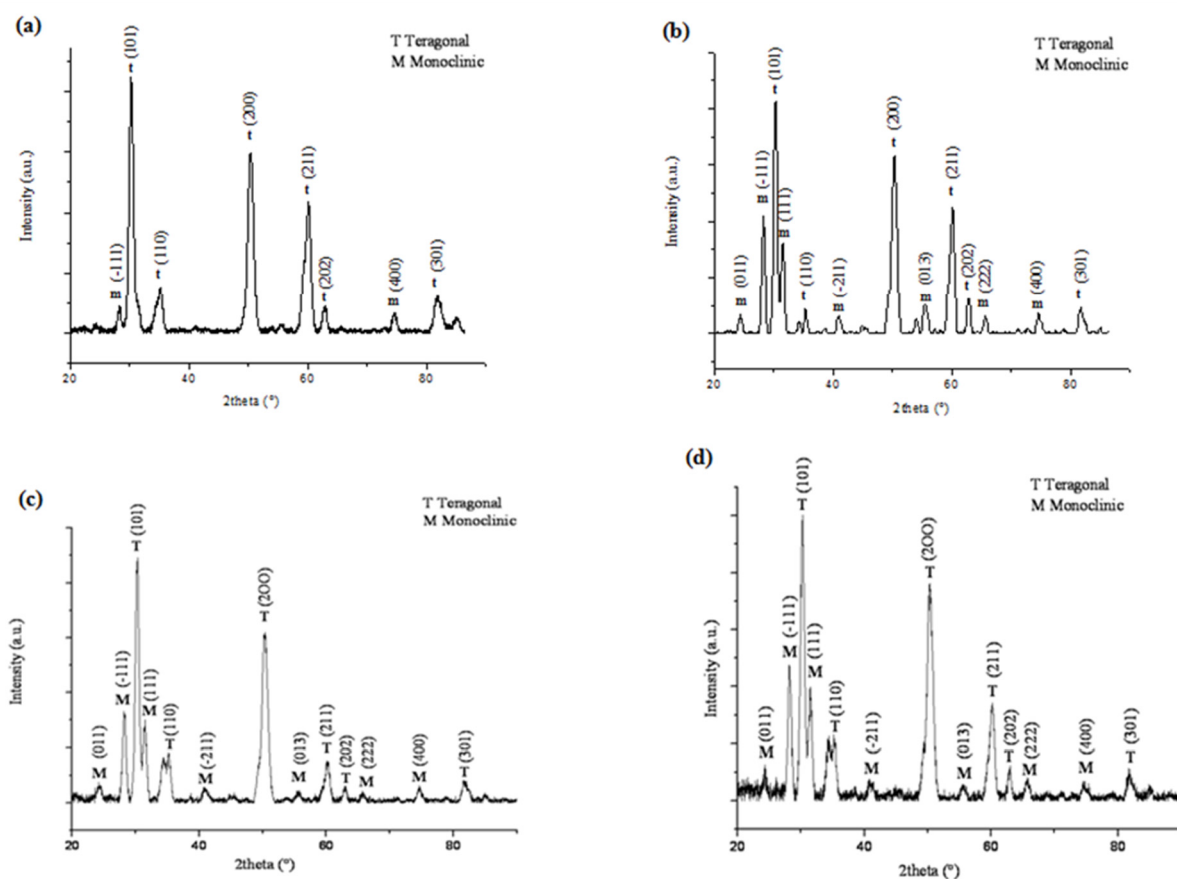
Figure 1. XRD patterns of (a) Zir-3/3-C, (b) Zir-2/4-C, (c) Zir-4/2-C, and (d) Zir-1/5-C.

microscopy (TEM) was conducted with a Tecnai G2 microscope at 120 kV. High-resolution TEM was carried out on a JEOL 2100F microscope, equipped with a high-resolution pole piece and field emission gun operating at 200 kV. Gas adsorption data in N_2 were collected using a Quantachrome Autosorb-1 automatic analyzer. Prior to N_2 sorption, all samples were degassed at 100 °C overnight under dynamic vacuum conditions. The specific surface areas were determined from the nitrogen adsorption/desorption isotherms at 77 K using the BET (Brunauer–Emmett–Teller) method. Pore size distributions were calculated from the N_2 adsorption isotherms with the "classic theory model" of Barrett, Joyner, and Halenda (BJH).[75]

X-ray photoelectron spectrosopy (XPS) studies were carried out in a Kratos Axis Ultra DLD spectrometer equipped with a monochromatic Al Kα X-ray source (hn = 1486.6 eV) operating at 150 W, a multichannel plate, and a delay line detector under 1.0×10^{-9} Torr vacuum. The survey and high-resolution spectra were collected at fixed analyzer pass energies of 160 and 20 eV, respectively. The instrument work function was calibrated to give an Au 4f7/2 metallic gold binding energy of 83.95 eV. The spectrometer dispersion was adjusted to give a binding energy of 932.63 eV for metallic Cu 2p3/2. Samples were mounted in floating mode to avoid differential charging. Charge neutralization was required for all samples. The electronic binding energy of C 1s (284.80 eV) was used as the internal standard. The data were analyzed with commercially available software, CasaXPS. The individual peaks were fitted by a Gaussian (70%)-Lorentzian (30%) (GL30) function after Shirley-type background subtraction.

2.5. Catalytic Activity Tests. In a typical experiment, LA (2 g, 0.017 mol), catalyst (25 mg), and ethanol, with LA/ethanol weight ratio was maintained at 1:5, were introduced into a two-necked round-bottom flask (50 mL) equipped with reflux condenser to perform the esterification reaction batchwise with magnetic stirring at 353 K for 8 h. The products were quantified using gas chromatography (Shimadzu GC-2014) equipped with a flame ionization detector (FID) and CP-Sil 43 CB column (25m × 0.25 mm). We analyzed some samples also by gas chromatography equipped with a mass spectrometry detector on GC-MS 1300/TSQ 8000 Evo THERMO.

3. RESULTS AND DISCUSSION

Zirconia nanoparticles with a controllable porosity were produced by micelle templating (sol–gel process) followed by a hydro-solvothermal treatment assisted by MW irradiation. The effects of urea, CTAB, and solvent ratio on morphology, structure, and pore size were investigated. The thermal stability of the zirconia samples was determined by TGA. At the calcination temperature of 500 °C, all samples were stable up to 1000 °C (as shown in Figure S1). The difference in weight loss between the samples is likely due to different amounts of urea used in the synthesis (0, 0.3, and 0.6 g). We reiterate that all the samples were washed and dried the same way. The sample prepared with higher urea mass showed the highest weight loss (35%), whereas the sample prepared without urea presented the lowest weight loss (15%). This difference can be explained by the variation of urea mass, which influences the rate of hydrolysis (key step of the sol–gel process).[76,77]

Table 1. Nanoparticle and Crystallite Sizes and Tetragonal Phase Percentage as a Function of Solvent Ratio (Cyclohexane/Water)

sample references	solvent ratio (mL/mL)	nanoparticle size (nm)[a]	crystallite size (nm)[b]	tetragonal phase (%)
Zir-5/1-C	50/10	15.2	14.4	55.76
Zir-4/2-C	40/20	13.8	12.1	63.24
Zir-3/3-C	30/30	12.1	10.6	86.26
Zir-2/4-C	20/40	14.9	13.5	57.50
Zir-1/5-C	10/50	13.3	12	58.42
Zir-0/6-C	0/60	12.4	10.5	80.6

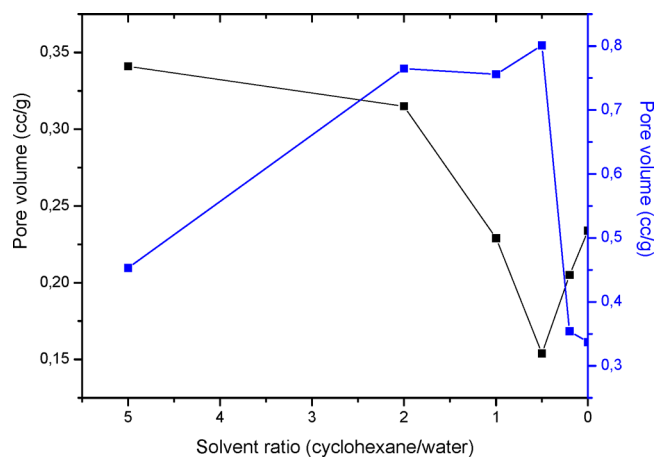[a]Evaluated by TEM. [b]Calculated by Debye−Scherrer equation.

Table 2. Surface Area, Pore Volume, and Pore Diameter as a Function of Solvent Ratio (Cyclohexane/Water) of Dried and Calcined Zirconia Nanoparticles

| sample references	BET (m^2/g)	pore volume (cm3/g)	pore diameter (nm)	C_{BET} parameter
Zir-5/1-D	438	0.453	3.83	59
Zir-5/1-C	57	0.341	17.81	129
Zir-4/2-D	401	0.765	3.82	63
Zir-4/2-C	51	0.315	12.28	109
Zir-3/3-D	240	0.756	3.5	65
Zir-3/3-C	38	0.229	15.29	132
Zir-2/4-D	193	0.801	3.81	67
Zir-2/4-C	37	0.154	9.94	113
Zir-1/5-D	305	0.354	3.79	69
Zir-1/5-C	39	0.205	12.31	122
Zir-0/6-D	149	0.337	3.85	66
Zir-0/6-C	48	0.234	9.56	125
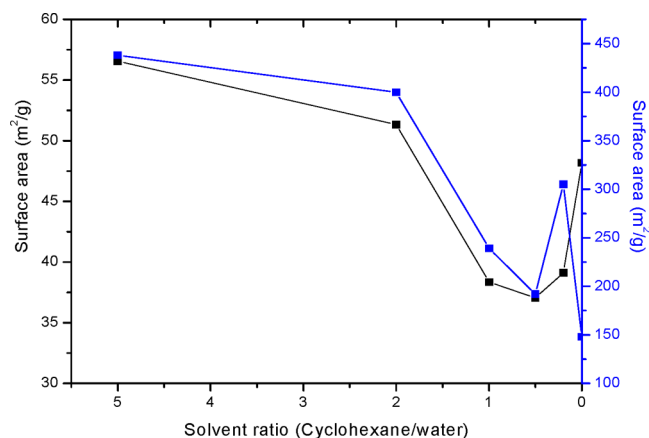
Figure 2. Surface area as a function of solvent ratio of dried noncalcined sample (blue curve) and calcined sample (black curve).


Figure 3. Pore volume as a function of solvent ratio of dried noncalcined sample (blue curve) and calcined sample (black curve).
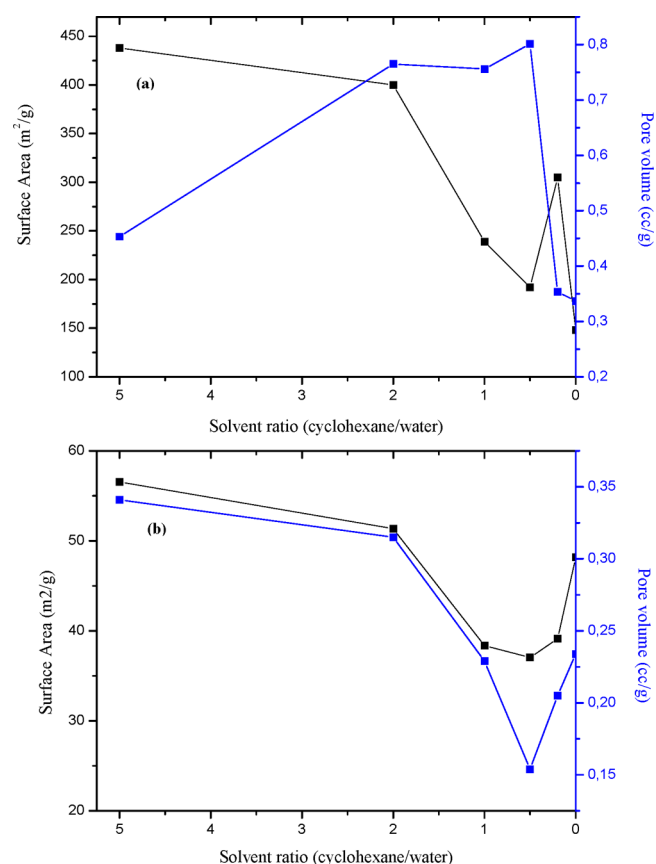

Figure 4. Surface area (black curve) and pore volume (blue curve) as a function of solvent ratio: (a) noncalcined sample and (b) sample calcined at 500 °C.

Indeed, these weight losses relate to organic residues generated during synthesis, as confirmed by the FTIR analysis of noncalcined and calcined samples. However, the analysis of these spectra, as shown in Figure S2, revealed that the noncalcined samples still contained organic residues, which had not been removed by washing. These spectra show the obvious presence of the absorption bands of −OH, −CH$_3$, and −CH$_2$−, which appear between 3450 and 3250 cm^{-1}, and between 2922 and 2847 cm^{-1}. A very intense band characteristic of a nitro alkane compound appears at 1576 cm^{-1}. Shown in Figure S3 is the probable structure of this molecule, 1-nitrohexadecane, which was formed by an oxidation reaction of quaternary ammonium under the

influence of MW irradiation. Furthermore, the absorption bands for other molecules (cyclohexane, urea, and CTAB) are not present. These findings were expected as it is quite usual to have organic residues in the synthesis of porous materials by the sol−gel process; this phenomenon remains a major challenge for chemists who synthesize porous oxides using organic templates. However, this analysis shows that the calcined sample does not present any absorption band pertaining to the organic substances. The urea helps to dissolve CTAB in water (0.012 mol in different volumes of
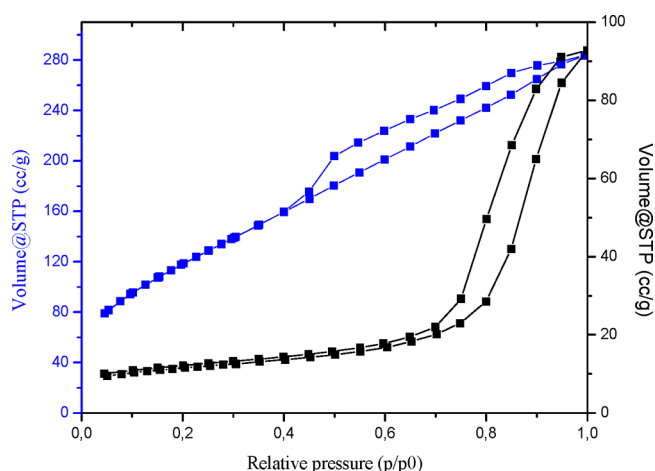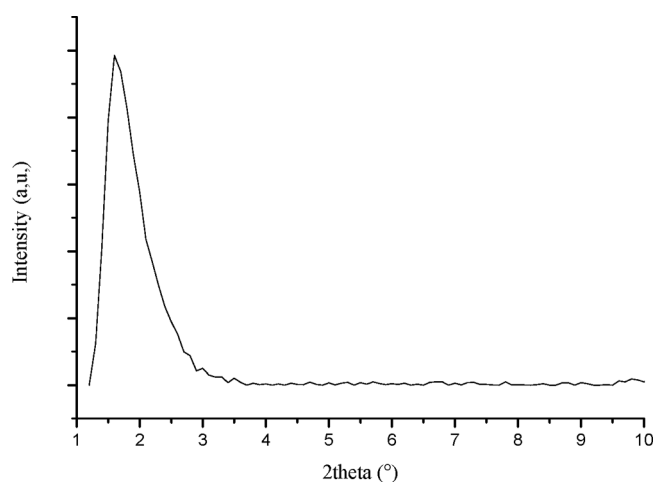
Figure 5. Nitrogen adsorption and desorption isotherms of representative samples prepared with solvent ratio 20/40 (cyclohexane/water): noncalcined sample (blue curve) and sample calcined at 500 °C (black curve).
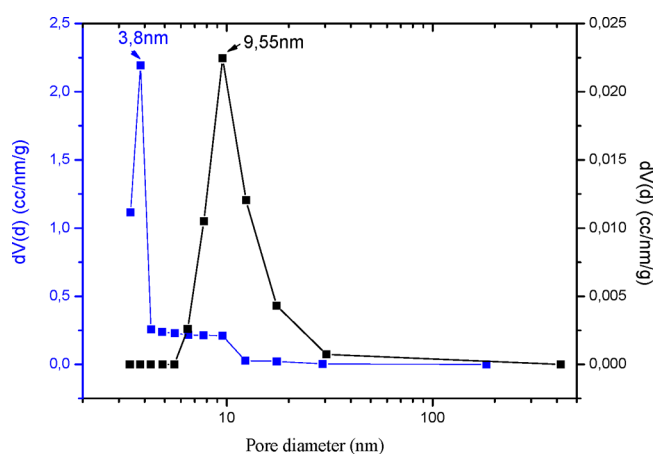
Figure 6. BJH pore size distribution of Zir-2/4-D (blue curve) and Zir-2/4-C (black curve).

Figure 7. Small-angle X-ray scattering spectrum of Zir-2/4-C.

water) because the concentration of CTAB was varied from 56 CMC (critical micellar concentration) to 280 CMC. The solution is formed by micelles or reverse micelles, according to the concentration of CTAB and the solvent ratio. Thus,

different forms and phases of micelle can be present; however, the assumption of the micelles being spherical seems reasonable.

The pore diameter for all dried samples was determined to be about 3.8 nm (vide infra). This value is consistent with the micelle diameter of the CTAB, which is approximately 4 nm (fully stretched surfactant chain is estimated to be 2.2 nm).[78] A high urea concentration translates to a high rate of hydrolysis and condensation reaction of the precursor, which traps the surfactant in closed volumes, forming an inaccessible medium for washing. Nitrogen adsorption/desorption analysis supports this conclusion by elucidating pore morphology and size for the noncalcined samples. This observation led us to keep the urea mass at 0.6 g and CTAB mass at 1 g, in this original study, in order to obtain amorphous dried zirconia nanoparticles with high organic residue trapped inside the amorphous structure. Thus, during the remainder of this study, the solvent ratio was varied from 50/10 to 0/60 (cyclohexane/water) for the sake of comparison, while keeping the concentrations of CTAB and urea constant. Figure 1 presents the XRD patterns of representative calcined samples. After calcination, all samples show a mixture of tetragonal and monoclinic phases with different proportions. The peaks are relatively broad, which is characteristic of nanocrystalline particles. The molar fraction of the tetragonal phase is calculated from the equation:[79]

$$\frac{M_{\mathrm{m}}}{M_{\mathrm{t}}} = 0.82 \times \frac{I_{\mathrm{m}}(-111) + I_{\mathrm{m}}(111)}{I_{\mathrm{t}}(101)} \tag{1}$$

where M_{m} and M_{t} are the molar ratios of monoclinic and tetragonal phases, and I_{m} and I_{t} are the intensities (as areas) of the peaks for the monoclinic and tetragonal phase. The factor 0.82 is a correction that takes into account the different structure factors of the two phases. Table 1 summarizes the influence of the solvent ratio on nanoparticle mean size, crystallite size, and tetragonal phase percentage. The solvent ratio has a small but significant effect on the average size of nanoparticles, which increased from 12.4 to 15.2 nm as the fraction of cyclohexane used during the synthesis was decreased. The sample Zir- 3/3-C has the highest percentage of tetragonal phase, which is the most sought after because of its role in important applications.[80] This 86% tetragonal phase sample has the smallest nanoparticle/crystallites, a finding consistent with previously reported data.[81] The Zir-3/3- C and Zir-0/6-C samples exhibit the highest percentage of tetragonal phase (86% and 80%, respectively), with a crystallite size of about 10.6 and 10.5 nm, respectively. The solvent mixture used in the preparation of Zir-3/3-C comprises water and hexane, thus causing ambiguity about the presence of a colloidal structure and micelle or reverse micelle; we reasoned it to be a micelle strictly on the basis of the morphology of the synthesized materials. The synthesis of Zir-0/6-C involves formation of a simple micelle acting as nanoreactor; micelles allow the growth of uniformly small nanoparticles that lead to samples with a higher percentage of tetragonal phase.

Table 2 gives the physical properties of the dried noncalcined and calcined zirconia nanoparticles. The surface areas ranged from 149 to 438 m^2/g for the noncalcined samples and 37 to 57 m^2/g for the calcined materials. The highest surface areas were observed for samples Zir-5/1-D (438 m^2/g) and Zir-5/1-C (56.5 m^2/g), prepared with a solvent ratio of 50/10. We can tentatively conclude that the higher surface area was obtained when the cyclohexane was
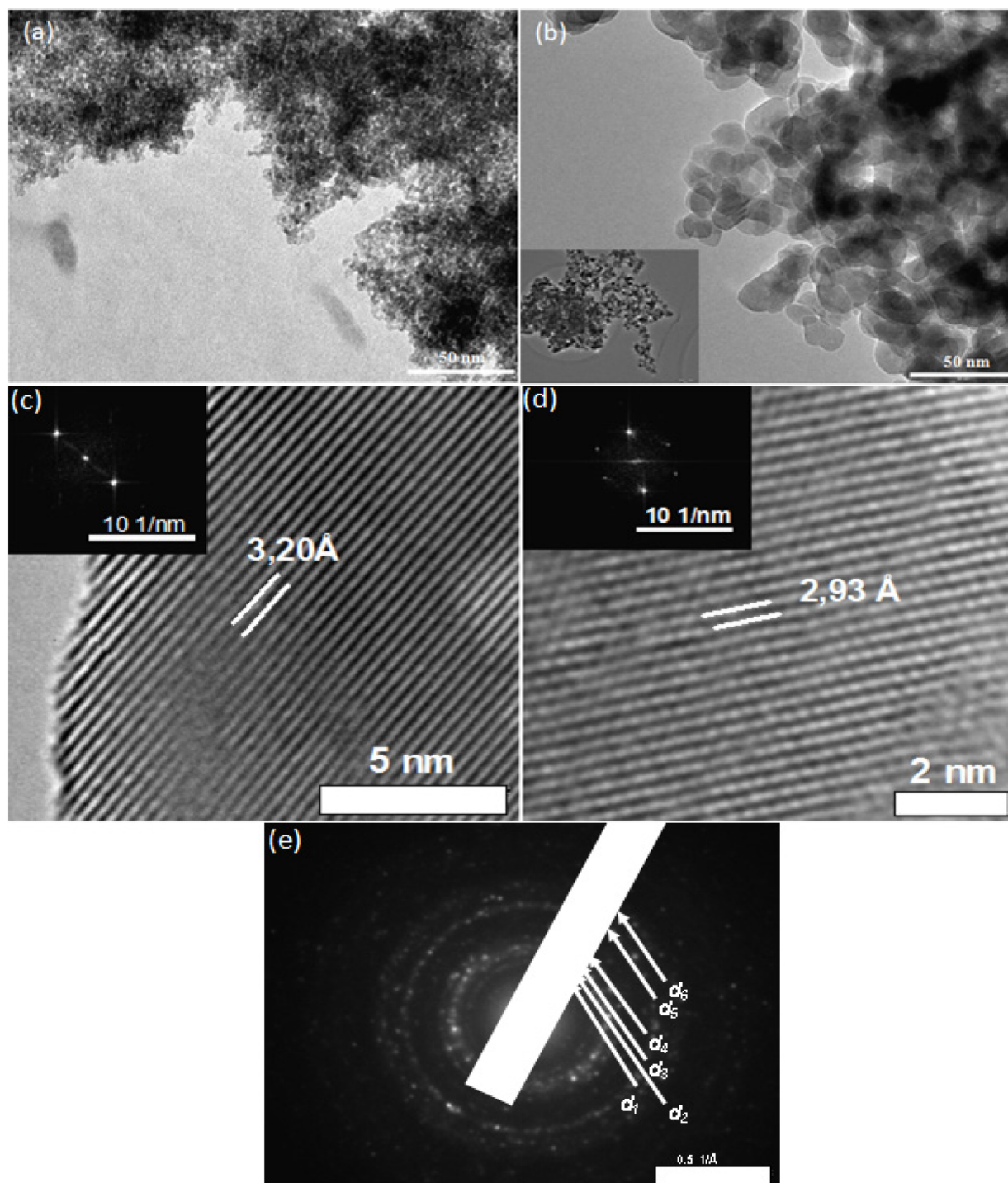
Figure 8. TEM images of zirconia nanoparticles: (a) Zir-2/4-D and (b) Zir-2/4-C. High-resolution TEM images of Zir-2/4-C at the center of a nanoparticle and their corresponding fast Fourier transform (FFT) patterns consistent with (c) m-ZrO$_2$ (monoclinic) and (d) t-ZrO$_2$ (tetragonal). (e) Corresponding selected area electron diffraction (SAED) pattern of Zir-2/4-C, where d_1 = 3.70 ± 0.02 Å, d_2 = 3.20 ± 0.02 Å, d_3 = 2.94 ± 0.02 Å, d_4 = 2.67 ± 0.02 Å, d_5 = 1.85 ± 0.02 Å, and d_6 = 1.57 ± 0.02 Å.

used. This could be explained by the stability of colloidal particles within aqueous nanoreactors formed when water molecules are trapped inside the organic solvent (cyclohexane) with the help of CTAB. The largest pore size (17.81 nm) occurred for Zir-5/1- C, which also has the highest surface area for the calcined samples. Surface area is usually inversely proportional to the pore diameter, but in fact it also depends on pore volume.[82] In this case, the Zir-5/1-C sample also has the highest pore volume measured for the calcined samples, 0.341 cm^3/g. The lowest surface area value was 37 m^2/g, which was observed for Zir-2/4-C.

The BET surface areas of the dried noncalcined and calcined zirconia nanoparticles are shown as a function of solvent ratio in Figure 2. Both types of samples showed the same variation of surface areas, except for the dried sample corresponding to a 0/60 solvent ratio. These results suggest that there was a
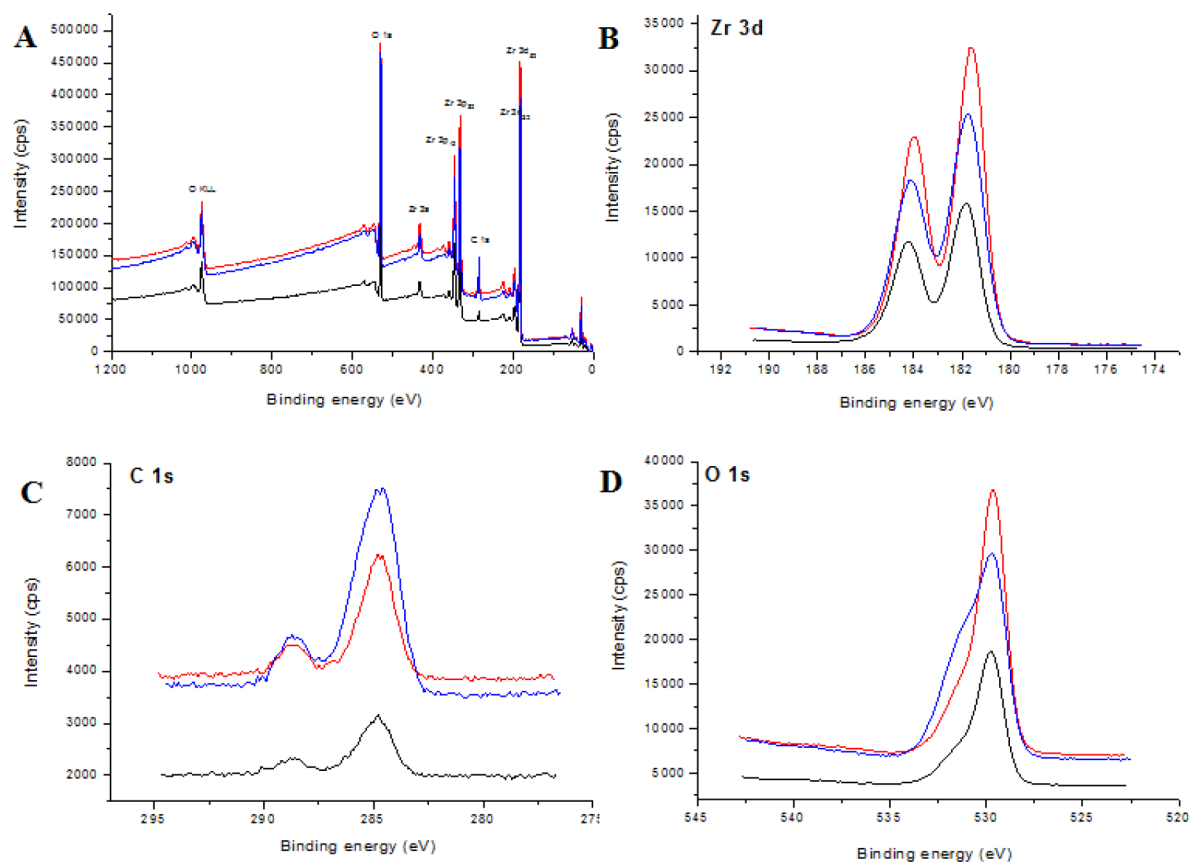
Figure 9. (A) XPS survey spectra of Zir-2/4-C (black curve), Zir-5/1-C (blue curve), and Zir-0/6-C (red curve); (B−D) high-resolution XPS spectra of C 1s, Zr 3d, and O 1s in these samples.
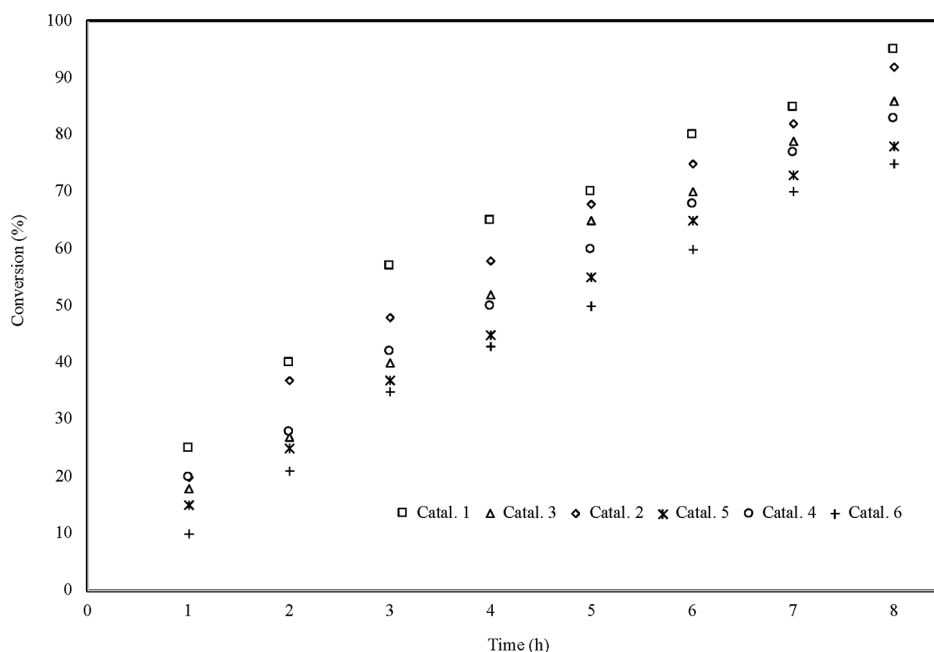
Figure 10. Catalytic screening into levulinic acid esterification with ethanol by using Zir-5/1-C@SO$_4^{2-}$ (Catal. 1), Zir-4/2-C@SO$_4^{2-}$ (Catal. 2), Zir-3/3-C@SO$_4^{2-}$ (Catal. 3), Zir-2/4-C@SO$_4^{2-}$ (Catal. 4), Zir-1/5-C@SO$_4^{2-}$ (Catal. 5), and Zir-0/6-C@SO$_4^{2-}$ (Catal. 6), respectively.

threshold of solvent ratio in which the surface area attained the lowest value at cyclohexane/water ratio of 0.5. To confirm this result, we prepared a sample with the same solvent ratio but half of the amount of CTAB (0.5 g) and urea (0.3 g).

The BET surface area of this sample after calcination was 36.49 m^2/g, which is consistent with that of Zir-2/4-C. Under this synthesis condition, the solvent ratio seems to play a key role on the surface area, originating from the aforementioned colloidal structure of the reaction media. In addition, the same

parameter seems to influence the pore volume, as presented in Figure 3. The data in Figure 3 indicate that the noncalcined and calcined samples follow opposite trends. When the solvent ratio decreased from 5 to 0.5, pore volume of the noncalcined samples increased while that of calcined samples decreased. These two curves suggest pore volume collapse because of heat treatment[83] and Ostwald ripening[84] for the noncalcined and calcined samples, respectively. These opposite trends can be explained by the effect of solvent ratio on the mesostructured and nanoparticle aggregation, since particle size does not differ significantly before calcination.

According to this result, when the solvent ratio is high, the nanoparticles are highly aggregated before calcination. However, these aggregated nanoparticles can easily be sintered by heat treatment at 500 °C, and as a result, the surface area is relatively higher compared to samples with lower solvent ratio (cyclohexane/water). Figure 4 shows the changes of pore volume and surface area for the noncalcined and calcined samples as a function of solvent ratio. Pore volume and surface area show opposite trends for the noncalcined sample and similar trends for the calcined sample.

Figure 5 presents nitrogen adsorption/desorption isotherms of Zir-2/4-D (blue curve) and Zir-2/4-C (black curve), which can be assigned to Type IV and Type V adsorption, respectively, according to the IUPAC classification.[85] The presence of hysteresis loops in both isotherms indicates capillary condensation in the mesopores. The closure of the loop observed at $P/P_0 = 0.4$ for the noncalcined sample suggests the presence of small mesopores. This is consistent with the finding that the average pore size for Zir-2/4-D was estimated to be 3.81 nm via the BJH technique (Table 2). In fact, all noncalcined samples show almost the same average pore size, but their pore distributions are different (Figures A4−A8), which originates from CTAB surfactant templating. The adsorption/desorption isotherm of the calcined sample, Zir-2/4-C, as shown in Figure 5 (black curve), is different from that of the noncalcined sample and estimated to be Type V. The hysteresis loop confirms that the calcined material kept its mesoporous structure after calcination. Hysteresis loops are classified into four types (H1 to H4) according to IUPAC classification,[86] and the loop shape seen in Figure 5 (blue curve) is of type H1, which has the attribute of uniform pores. The formation of pores for this reference sample can be explained by crystallization (of the wall) of the amorphous zirconia leading to formation of well-arranged crystallites and Ostwald ripening. Removal of organic residues assists the activation of these phenomena.

Figure 6 shows the BJH pore size distributions of the noncalcined (blue curve) and calcined samples prepared with a solvent ratio of 20/40. The narrow pore size distribution is clearly observed in this figure; the peak is centered at 9.55 nm for the calcined sample, with a full width at half-maximum (fwhm) of about 5.09 nm. Many research groups have focused on stabilizing this narrow-size mesopore distribution at relatively high temperature. A number of methods have been explored but failed to avoid collapse of mesopores after calcination. It appears that the method used here (changing the solvent ratio) is a simple and straightforward approach that helps maintain a pore structure after calcination (Figures S5−S8).

In general, depending on the nature of the porosity, we can classify the materials into three main groups: (i) the pores are formed by the spatial arrangement of small solid particles of different shapes (micro- or nanoparticles), and their aggregation leads to intergranular porosity; (ii) the pores are channels or cavities formed by soft surfactant templates, and the solidification of surfactant templates and their extraction give rise to a meso- or macro- porosity; and (iii) the pores are channels within the mesh of zeolitic-type crystalline material, which generates structural microporosity. Keep in mind that the samples prepared in this work are assumed to be filled with surfactant, which implies that the only accessible porosity must be around or between the zirconia particles. Unlike the mechanism of formation of MCM-41, for which the specific surface areas before calcination are very low, here we demonstrate the formation of noncalcined porous materials (see nonisothermal samples calcined in the Supporting Information). We procured mesoporous oxides before calcination, with specific surface areas comparable to those obtained with calcined silica MCM-41, as well as hysteresis loops which are situated at high pressure (P/P_0 of = 0.5 to 0.9). These noncalcined samples have a calibrated and uniform mesoporous structure with a pore diameter of 3.8 nm. The CBET parameter values of the samples are all about 60−70 (Table 2), typical of mesoporous materials. These results indicate the presence of surfactant around the particles of zirconium oxide, leading to a lower interaction of the surfactant to the nitrogen oxide than for zirconium.

The oxides after calcination have specific surface areas less than the noncalcined samples, and the C_{BET} parameters are higher after calcination. These findings reflect better interaction between nitrogen and zirconium oxide after calcination, which can be rationalized by crystallization of the material. However, the shape of the isotherms of adsorption/desorption of the calcined samples is not the same as before calcination. This finding can be explained by a change of the mechanism of nitrogen adsorption/desorption and then a difference of porous structure before and after calcination. In addition, the hysteresis loop for the calcined sample appears at higher pressures, probably due to the filling of mesopores, insofar as a well-defined plateau is present at saturation ($P/P_0 = 0.90$ to 0.99). We can offer two possibilities for this phenomenon. The first is that the calcination removed the surfactant, which is located around the zirconia particles, and left a larger interstitial space for nitrogen molecules. The second is that the surfactant is located around, but also within, the particles so that the calcination leads to an interparticle porosity and a cylindrical pore. In any case, the interaction between the surfactant and the zirconia should be high enough that the surfactant remains adsorbed, despite successive washes after synthesis. We believe that the second hypothesis is most plausible, since the isothermal adsorption/desorption curves before and after calcination are significantly different and the pore diameter is significantly increased after calcination.

Small-angle X-ray scattering of Zir-2/4-C shows only one broad peak at 1.6°, corresponding to a spacing distance of 5.5 nm Figure 7. The intensity of the principal peak (100) can be attributed to a slight change in the periodical distance (less regular stacking) or the small size of organized monodomains. The absence of other peaks [(210), (110), and (200)] is an indication of hexagonal lattice distortion.

In Figure 8, the TEM images for Zir-2/4-D and Zir-2/4-C show that the zirconia nanoparticles are spherical or egg-shaped. As shown in Figure 8a, the noncalcined sample (Zir-2/4-D) has aggregated nanoparticles with an average diameter of 2.8 nm surrounded by organic residues. This observation was

confirmed by TGA analysis, which showed that this sample still contains 15% by weight of organic residue. In fact, during heat treatment, nanoparticles tended to agglomerate and thereby form bigger particles (13.5 nm). This process can be explained by the crystallization mechanism and Ostwald ripening inhibition, which allow stabilization of relatively smaller aggregated nanoparticles Figure 8b. The particle size evaluated by TEM is larger than the crystallite size calculated from the Debye–Scherrer equation. This difference may be due to the crystallites having an egg-shaped morphology and the Debye–Scherer formula providing a roughly averaged size in the three directions. The high-resolution TEM images in Figure 8c,d indicate good crystallinity. The lattice spacings were determined to be 3.20 and 2.93 Å, which correspond to the lattice $d_{(-111)}$ and $d_{(101)}$ interplanar spacing of monoclinic and tetragonal phases, respectively. Furthermore, the SAED pattern in Figure 8e confirms the presence of polycrystalline tetragonal and monoclinic phases. These analyses corroborate the XRD analysis.

Figure 9A presents XPS curves of representative samples of Zir-2/4-C, Zir-1/5-C, and Zir-0/6-C. The three major peaks corresponding to Zr (Zr 3d), O (O 1s), and C (C 1s) are clearly observed. The presence of the C 1s peak in the spectra is due to atmospheric contaminants and residual carbon remaining after heat treatment. (Figure 9B–D) display the high-resolution XPS spectra of the Zr 3d, O 1s, and C 1s core levels. The measured Zr/O ratio is about 1:2, which is consistent with the theoretical ratio for ZrO_2. The peaks located at 181.9 and 184.3 eV can be assigned to the spin–orbit splitting of the Zr 3d components (Zr $3d_{5/2}$ and Zr $3d_{3/2}$). The binding energy of the main peak of O 1s is located at 530.0 eV, corresponding to oxygen in ZrO_2.[36,87,88] The peak positions of Zr 3d and O 1s core levels and their relative intensities are basically similar for the three samples and consistent with the literature data for ZrO_2.[89–91]

Sulfated mesoporous nanostructured zirconia performances were evaluated in the esterification of levulinic acid with ethanol. First, the test results show that the nonsulfated zirconia samples are very low catalytic activity which does not exceed 2% after 8 h of reaction. It was noted further that the zirconia samples sulfation leads to a significant increase in the catalytic activity (Figure 10). The only registered products are ethyl levulinate and water. The conversions of LA to ethyl levulinate after 8 h of reaction are 95, 92, 86, 83, 78, and 75% by using Zir-5/1-C@SO_4^{2-}, Zir-3/3-C@SO_4^{2-}, Zir-4/2-C@SO_4^{2-}, Zir-1/5-C@SO_4^{2-}, Zir-2/4-C@SO_4^{2-}, and Zir-0/6-C@SO_4^{2-}, respectively. Thus, Zir-5/1-C@SO_4^{2-} shows increased catalytic activity in comparison with other catalysts. Zir-5/1-C@SO_4^{2-} has the specific surface area of around 57 m²/g and the pore diameter of 17.81 nm; notably, it has the largest pore diameter. This result could be attributed to the calibrated mesoporosity of this sample assuring the easier molecular circulation throughout catalytic cycle.[73,74] Those results show that the catalytic performances of the sulfated oxides are closely related to the porosities of the nonsulfated oxides. The use of mesoporous nanostructured zirconia, to have sulfated samples, increases the rate of active sites providing the excellent catalytic performance of those catalysts in this chemical transformation. It should be noted, however, that our catalysts are more or less comparable with similar ones already published.[69–71]

4. CONCLUSIONS

Novel mesoporous particles of zirconia with narrow size distribution have been successfully synthesized via a sol–gel process followed by hydro-solvothermal treatment under microwave irradiation. We have shown that controlling the solvent ratio leads to well-organized nanoparticle aggregates after calcination, which results in the formation of thermally stable mesoporous materials. Thus, mesoporous zirconia with well-controlled pore size, well- organized structure and distribution was synthesized by adopting this suitable and versatile route. The average pore size may range from 9.55 to 17.81 nm. Indeed, pore size affects the catalytic properties of those oxides after their sulfating. Sulfated mesoporous nanostructured zirconia showed the highest catalytic perform- ances regarding the heterogeneous esterification of levulinic acid by ethanol giving rise to ethyl levulinate. A conversion of 95% was obtained by the catalytic action of the sample Zir-5/ 1-C@SO_4^{2-} (cyclohexane/water: 50/10 mL/mL) after 8 h of the reaction at 80 °C. These results clearly demonstrate that this oxides synthesis route we have developed provides a new approach to the design and preparation of mesoporous and nanostructured catalysts with expected performance to produce molecules of high added value. However, these encouraging preliminary results have led to an important ongoing work in point of view on catalytic processes.

■ ASSOCIATED CONTENT

Ⓢ Supporting Information

The Supporting Information is available free of charge at https://pubs.acs.org/doi/10.1021/acsomega.2c00060.

> Thermogravimetric analysis, FTIR spectra of dried sample, X-ray diffraction patterns of some representative samples, additional pore size distributions, and TEM pictures (PDF)

■ AUTHOR INFORMATION

Corresponding Author

Abdellatif Barakat − UMR IATE, University of Montpellier, INRAE, Agro Institute Montpellier, 34060 Montpellier, France; Mohamed VI Polytechnic University, 43150 Ben Guerir, Morocco; ◉ orcid.org/0000-0003-4196-4351; Email: abdellatif.barakat@inrae.fr

Authors

Salaheddine Lanaya − UMR IATE, University of Montpellier, INRAE, Agro Institute Montpellier, 34060 Montpellier, France; Organic Chemistry and Analytical Laboratory, FST, University of Sultane Moulay Slimane, Béni-Mellal 23000, Morocco

Yousra El Jemli − IMED-Lab, FST, Cadi Ayyad University, 40000 Marrakech, Morocco

Khadija Khallouk − UMR IATE, University of Montpellier, INRAE, Agro Institute Montpellier, 34060 Montpellier, France; LMPCE, EST, Université Sidi Mohammed Ben Abdellah, 30000 Fes, Morocco; ◉ orcid.org/0000-0002-4919-8594

Karima Abdelouahdi − IMED-Lab, FST, Cadi Ayyad University, 40000 Marrakech, Morocco

Abdellah Hannioui − Organic Chemistry and Analytical Laboratory, FST, University of Sultane Moulay Slimane, Béni-Mellal 23000, Morocco

Abderrahim Solhy − *UMR IATE, University of Montpellier, INRAE, Agro Institute Montpellier, 34060 Montpellier, France*

Complete contact information is available at:
https://pubs.acs.org/10.1021/acsomega.2c00060

Author Contributions

All authors contributed equally to this work, and also to the writing of the manuscript. All authors have given approval to the final version of the manuscript.

Notes

The authors declare no competing financial interest.

◼ REFERENCES

(1) Kumari, L.; Du, G. H.; Li, W. Z.; Vennila, R. S.; Saxena, S. K.; Wang, D. Z. Synthesis, microstructure and optical characterization of zirconium oxide nanostructures. *Ceram. Int.* **2009**, *35*, 2401−2408.

(2) Wu, T.-S.; Wang, K.-X.; Zou, L.-Y.; Li, X.-H.; Wang, P.; Wang, D.-J.; Chen, J.-S. Effect of Surface Cations on Photoelectric Conversion Property of Nanosized Zirconia. *J. Phys. Chem. C* **2009**, *113*, 9114−9120.

(3) Lin, C.; Zhang, C.; Lin, J. Phase Transformation and Photoluminescence Properties of Nanocrystalline ZrO_2 Powders Prepared via the Pechini-type Sol−Gel Process. *J. Phys. Chem. C* **2007**, *111*, 3300−3307.

(4) Liang, J.; Deng, Z.; Jiang, X.; Li, F.; Li, Y. Photoluminescence of Tetragonal ZrO_2 Nanoparticles Synthesized by Microwave Irradiation. *Inorg. Chem.* **2002**, *41*, 3602−3604.

(5) Guzman, F.; Singh, R.; Chuang, S. S. C. Direct Use of Sulfur-Containing Coke on a Ni−Yttria-STableilized Zirconia Anode Solid Oxide Fuel Cell. *Energy Fuels* **2011**, *25*, 2179−2186.

(6) Kim, J.; Shin, D.; Son, J.-W.; Lee, J.-H.; Kim, B.-K.; Je, H.-J.; Lee, H.-W.; Yoon, K. J. Fabrication and characterization of all-ceramic solid oxide fuel cells based on composite oxide anode. *J. Power Sources* **2013**, *241*, 440−448.

(7) Wang, S. F.; Zhang, J.; Luo, D. W.; Gu, F.; Tang, D. Y.; Dong, Z. L. Transparent ceramics: Processing, materials and applications. *Progress in Solid State Chemistry* **2013**, *41*, 20−54.

(8) Zhao, J.; Shen, Z.; Si, W.; Wang, X. Bi-colored zirconia as dental restoration ceramics. *Ceram. Int.* **2013**, *39*, 9277−9283.

(9) Huang, Y. L.; Lee, Y. C.; Tsai, D. C.; Chiu, J. D.; Shieu, F. S. Effects of manganese oxide addition and reductive atmosphere annealing on the phase stability and microstructure of yttria stabilized zirconia. *J. Eur. Ceram. Soc.* **2013**, *33*, 2609−2615.

(10) Ramu, P.; Saravanan, C. G. Investigation of Combustion and Emission Characteristics of a Diesel Engine with Oxygenated Fuels and Thermal Barrier Coating. *Energy Fuels* **2009**, *23*, 653−656.

(11) Pin, L.; Pilgrim, C.; Feist, J.; Le Maoult, Y.; Ansart, F.; Lours, P. Characterisation of thermal barrier sensor coatings synthesised by sol-gel route. *Sensors Actuators A Phys.* **2013**, *199*, 289−296.

(12) Steiner, S. A.; Baumann, T. F.; Bayer, B. C.; Blume, R.; Worsley, M. A.; MoberlyChan, W. J.; Shaw, E. L.; Schlogl, R.; Hart, A. J.; Hofmann, S.; Wardle, B. L. Nanoscale Zirconia as a Nonmetallic Catalyst for Graphitization of Carbon and Growth of Single- and Multiwall Carbon Nanotubes. *J. Am. Chem. Soc.* **2009**, *131*, 12144−12154.

(13) Wang, D.; Osmundsen, C. M.; Taarning, E.; Dumesic, J. A. Selective Production of Aromatics from Alkylfurans over Solid Acid Catalysts. *ChemCatChem.* **2013**, *5*, 2044−2050.

(14) Sato, A. G.; Volanti, D. P.; Meira, D. M.; Damyanova, S.; Longo, E.; Bueno, J. M. C. Effect of the ZrO2 phase on the structure and behavior of supported Cu catalysts for ethanol conversion. *J. Catal.* **2013**, *307*, 1−17.

(15) Wang, W.; Xie, Z.; Liu, G.; Yang, W. Fabrication of Blue-Colored Zirconia Ceramics via Heterogeneous Nucleation Method. *Cryst. Growth Des* **2009**, *9*, 4373−4377.

(16) Freris, I.; Riello, P.; Enrichi, F.; Cristofori, D.; Benedetti, A. Synthesis and optical properties of sub-micron sized rare earth-doped zirconia particles. *Opt. Mater. (Amst)* **2011**, *33*, 1745−1752.

(17) Cunha, C. d. S.; Ferrari, J. L.; de Oliveira, D. C.; Maia, L. J. Q.; Gomes, A. S. L.; Ribeiro, S. J. L.; Goncalves, R. R. NIR luminescent Er^{3+}/Yb^{3+} co-doped SiO_2-ZrO_2 nanostructured planar and channel waveguides: Optical and structural properties. *Mater. Chem. Phys.* **2012**, *136*, 120−129.

(18) Leroy, C.M.; Cardinal, T.; Jubera, V.; Aymonier, C.; Treguer-Delapierre, M.; Boissiere, C.; Grosso, D.; Sanchez, C.; Viana, B.; Pelle, F. Luminescence properties of ZrO_2 mesoporous thin films doped with Eu3+ and Agn. *Microporous Mesoporous Mater.* **2013**, *170*, 123−130.

(19) Sharma, P. K.; Saxena, N.; Bhatt, A.; Rajagopal, C.; Roy, P. K. Synthesis of mesoporous bimetallic Ni-Cu catalysts supported over ZrO_2 by a homogenous urea coprecipitation method for catalytic steam reforming of ethanol. *Catal. Sci. Technol.* **2013**, *3*, 1017−1026.

(20) Tyagi, B.; Sidhpuria, K.; Shaik, B.; Jasra, R. V. Synthesis of Nanocrystalline Zirconia Using Sol−Gel and Precipitation Techniques. *Ind. Eng. Chem. Res.* **2006**, *45*, 8643−8650.

(21) Zhang, L.; Hao, S.; Liu, B.; Shum, H. C.; Li, J.; Chen, H. Fabrication of Ceramic Microspheres by Diffusion-Induced Sol-Gel Reaction in Double Emulsions. *ACS Appl. Mater. Interfaces* **2013**, *5*, 11489−11493.

(22) Hornebecq, V.; Knöfel, C.; Boulet, P.; Kuchta, B.; Llewellyn, P. L. Adsorption of Carbon Dioxide on Mesoporous Zirconia: Microcalorimetric Measurements, Adsorption Isotherm Modeling, and Density Functional Theory Calculations. *J. Phys. Chem. C* **2011**, *115*, 10097−10103.

(23) Li, W.; Huang, H.; Li, H.; Zhang, W.; Liu, H. Facile Synthesis of Pure Monoclinic and Tetragonal Zirconia Nanoparticles and Their Phase Effects on the Behavior of Supported Molybdena Catalysts for Methanol-Selective Oxidation. *Langmuir* **2008**, *24*, 8358−8366.

(24) Wang, M. C.; Huang, H. J. Crystallization behavior of tetragonal ZrO2 prepared in a silica bath. *Thermochim. Acta* **2013**, *567*, 93−99.

(25) Song, Y. Q.; Liu, H. M.; He, D. H. Effects of Hydrothermal Conditions of ZrO_2 on Catalyst Properties and Catalytic Performances of Ni/ZrO_2 in the Partial Oxidation of Methane. *Energy Fuels* **2010**, *24*, 2817−2824.

(26) Ávila Brande, D.; Perezzan, R.; Urones-Garrote, E.; Otero-Díaz, L. C. Chlorination and Solvothermal Treatment of $Zr(C_5H_5)_2Cl_2$: a Synthetic Combination to Produce Nanometric Tetragonal ZrO_2. *Inorg. Chem.* **2011**, *50*, 4640−4646.

(27) Tartaj, P.; Bomati-Miguel, O.; Rebolledo, A. F.; Valdes-Solis, T. Controlled release of precipitating agents through solvothermal desTableilization of microemulsions: one-pot synthesis of monoclinic zirconia nanostructures. *J. Mater. Chem.* **2007**, *17*, 1958−1963.

(28) Palkovits, R.; Kaskel, S. Reverse micelle-mediated synthesis of zirconia with enhanced surface area using alcothermal treatment. *J. Mater. Chem.* **2006**, *16*, 391−394.

(29) Chen, L.; Mashimo, T.; Omurzak, E.; Okudera, H.; Iwamoto, C.; Yoshiasa, A. Pure Tetragonal ZrO_2 Nanoparticles Synthesized by Pulsed Plasma in Liquid. *J. Phys. Chem. C* **2011**, *115*, 9370−9375.

(30) Gröhn, A. J.; Pratsinis, S. E.; Wegner, K. Fluid-particle dynamics during combustion spray aerosol synthesis of ZrO_2. *Chem. Eng. J.* **2012**, *191*, 491−502.

(31) Vallet-Regi, M.; Nicolopoulos, S.; Roman, J.; Martinez, J. L.; Gonzalez-Calbet, J. M. Structural characterization of ZrO2 nanoparticles obtained by aerosol pyrolysis. *J. Mater. Chem.* **1997**, *7*, 1017−1022.

(32) Ramananarivo, H. R.; Abdelouahdi, K.; Amer, W.; Zahouily, M.; Clark, J.; Solhy, A. Tunable Structure of Zirconia Nanoparticles

by Biopolymer Gelation: Design, Synthesis and Characterization. *Eur. J. Inorg. Chem.* **2012**, *2012*, 5465−5469.

(33) Bai, L.; Wyrwalski, F.; Machut, C.; Roussel, P.; Monflier, E.; Ponchel, A. Hydroxypropyl-[small beta]-cyclodextrin as a versatile additive for the formation of metastable tetragonal zirconia exhibiting high thermal stability. *CrystEngComm* **2013**, *15*, 2076−2083.

(34) Jiang, Y.; Yang, D.; Zhang, L.; Jiang, Y.; Zhang, Y.; Li, J.; Jiang, Z. Facile Synthesis and Novel Application of Zirconia Catalyzed and Templated by Lysozyme. *Ind. Eng. Chem. Res.* **2008**, *47*, 1876−1882.

(35) Bansal, V.; Rautaray, D.; Ahmad, A.; Sastry, M. Biosynthesis of zirconia nanoparticles using the fungus Fusarium oxysporum. *J. Mater. Chem.* **2004**, *14*, 3303−3305.

(36) Tang, S.; Huang, X.; Chen, X.; Zheng, N. Hollow Mesoporous Zirconia Nanocapsules for Drug Delivery. *Adv. Funct. Mater.* **2010**, *20*, 2442−2447.

(37) Subramanian, A.; Sarkar, S. Use of a modified zirconia support in the separation of immunoproteins. *J. Chromatogr. A* **2002**, *944*, 179−187.

(38) Trens, P.; Stichert, W.; Hudson, M. J. Formation of high surface area mesoporous zirconias. *J. Chim. Phys. PHYSICO-CHIMIE Biol.* **1998**, *95*, 2034−2047.

(39) Vantomme, A.; Yuan, Z. Y.; Su, B. L. One-pot synthesis of a high-surface-area zirconium oxide material with hierarchically three-length-scaled pore structure. *New J. Chem.* **2004**, *28*, 1083−1085.

(40) Yang, D.; Qi, L.; Ma, J. Hierarchically ordered networks comprising crystalline ZrO_2 tubes through sol-gel mineralization of eggshell membranes. *J. Mater. Chem.* **2003**, *13*, 1119−1123.

(41) Parvulescu, V.I; Bonnemann, H; Parvulescu, V; Endruschat, U; Rufinska, A; Lehmann, C. W.; Tesche, B; Poncelet, G Preparation and characterisation of mesoporous zirconium oxide. *Appl. Catal. A Gen* **2001**, *214*, 273−287.

(42) Blin, J.-L.; Leonard, A.; Yuan, Z.-Y.; Gigot, L.; Vantomme, A.; Cheetham, A. K.; Su, B.-L. Hierarchically mesoporous/macroporous metal oxides templated from polyethylene oxide surfactant assemblies. *Angew. Chem.* **2003**, *115*, 2978−2981.

(43) Deshmane, V. G.; Adewuyi, Y. G. Synthesis of thermally sTable, high surface area, nanocrystalline mesoporous tetragonal zirconium dioxide (ZrO 2): effects of different process parameters. *Microporous Mesoporous Mater.* **2012**, *148*, 88−100.

(44) Mishra, M. K.; Tyagi, B.; Jasra, R. Effect of synthetic parameters on structural, textural, and catalytic properties of nanocrystalline sulfated zirconia prepared by sol-gel technique. *Ind. Eng. Chem. Res.* **2003**, *42*, 5727−5736.

(45) Sun, Y.; Ma, S.; Du, Y.; Yuan, L.; Wang, S.; Yang, J.; Deng, F.; Xiao, F.-S. Solvent-free preparation of nanosized sulfated zirconia with Brønsted acidic sites from a simple calcination. *J. Phys. Chem. B* **2005**, *109*, 2567−2572.

(46) Althues, H.; Kaskel, S. Sulfated zirconia nanoparticles synthesized in reverse microemulsions: preparation and catalytic properties. *Langmuir* **2002**, *18*, 7428−7435.

(47) Das, S. K.; Bhunia, M. K.; Sinha, A. K.; Bhaumik, A. Self-assembled mesoporous zirconia and sulfated zirconia nanoparticles synthesized by triblock copolymer as template. *J. Phys. Chem. C* **2009**, *113*, 8918−8923.

(48) Chen, S. Y.; Jang, L. Y.; Cheng, S. Synthesis of thermally sTable zirconia-based mesoporous materials via a facile post-treatment. *J. Phys. Chem. B* **2006**, *110*, 11761−11771.

(49) Rao, K. J.; Vaidhyanathan, B.; Ganguli, M.; Ramakrishnan, P. A. Synthesis of inorganic solids using microwaves. *Chem. Mater.* **1999**, *11*, 882−895.

(50) Kitchen, H. J.; Vallance, S. R.; Kennedy, J. L.; Tapia-Ruiz, N.; Carassiti, L.; Harrison, A.; Whittaker, A. G.; Drysdale, T. D.; Kingman, S. W.; Gregory, D. H. Modern microwave methods in solid-state inorganic materials chemistry: from fundamentals to manufacturing. *Chem. Rev.* **2014**, *114*, 1170−1206.

(51) Dwivedi, R.; Maurya, A.; Verma, A.; Prasad, R.; Bartwal, K. S. Microwave assisted sol-gel synthesis of tetragonal zirconia nanoparticles. *J. Alloys Compd.* **2011**, *509*, 6848−6851.

(52) Li, C.; Li, K.; Li, H.; Zhang, Y.; Ouyang, H.; Liu, L.; Sun, C. Effect of reaction temperature on crystallization of nanocrystalline zirconia synthesized by microwave-hydrothermal process. *J. Alloys Compd.* **2013**, *561*, 23−27.

(53) Lomba, L.; Muniz, S.; Pino, M. R.; Navarro, E.; Giner, B. Ecotoxicity studies of the levulinate ester series. *Ecotoxicology* **2014**, *23*, 1484−1493.

(54) Bart, H. J.; Reidetschlager, J.; Schatka, K.; Lehmann, A. Kinetics of esterification of levulinic acid with n-butanol by homogeneous catalysis. *Ind. Eng. Chem. Res.* **1994**, *33*, 21−25.

(55) Sah, P. P. T.; Ma, S. Y. Levulinic acid and its esters. *J. Am. Chem. Soc.* **1930**, *52*, 4880−4883.

(56) Hishikawa, Y.; Yamaguchi, M.; Kubo, S.; Yamada, T. Direct preparation of butyl levulinate by a single solvolysis process of cellulose. *Journal of Wood Science* **2013**, *59*, 179−182.

(57) Fernandes, D.R.; Rocha, A.S.; Mai, E.F.; Mota, C.J.A.; Teixeira da Silva, V. Levulinic acid esterification with ethanol to ethyl levulinate production over solid acid catalysts. *Applied Catalysis A: General* **2012**, *425-426*, 199−204.

(58) Kuwahara, Y.; Fujitani, T.; Yamashita, H. Esterification of levulinic acid with ethanol over sulfated mesoporous zirconosilicates: Influences of the preparation conditions on the structural properties and catalytic performances. *Catal. Today* **2014**, *237*, 18−28.

(59) Patil, C. R.; Niphadkar, P. S.; Bokade, V. V.; Joshi, P. N. Esterification of levulinic acid to ethyl levulinate over bimodal micro-mesoporous H/BEA zeolite derivatives. *Catal. Commun.* **2014**, *43*, 188−191.

(60) Nandiwale, K. Y.; Pande, A. M.; Bokade, V. V. One step synthesis of ethyl levulinate biofuel by ethanolysis of renewable furfuryl alcohol over hierarchical zeolite catalyst. *RSC Adv.* **2015**, *5*, 79224−79231.

(61) Nandiwale, K. Y.; Niphadkar, P. S.; Deshpande, S. S.; Bokade, V. V. Esterification of renewable levulinic acid to ethyl levulinate biodiesel catalyzed by highly active and reusable desilicated H-ZSM-5. *J. Chem. Technol. Biotechnol.* **2014**, *89*, 1507−1515.

(62) Melero, J. A.; Morales, G.; Iglesias, J.; Paniagua, M.; Hernandez, B.; Penedo, S. Efficient conversion of levulinic acid into alkyl levulinates catalyzed by sulfonic mesostructured silicas. *Applied Catalysis A: General* **2013**, *466*, 116−122.

(63) Nandiwale, K. Y.; Bokade, V. V. Environmentally benign catalytic process for esterification of renewable levulinic acid to various alkyl levulinates biodiesel. *Environmental Progress & Sustainable Energy* **2015**, *34*, 795−801.

(64) Cirujano, F.G.; Corma, A.; Llabres i Xamena, F.X. Conversion of levulinic acid into chemicals: Synthesis of biomass derived levulinate esters over Zr-containing MOFs. *Chem. Eng. Sci.* **2015**, *124*, 52−60.

(65) Siva Sankar, E.; Mohan, V.; Suresh, M.; Saidulu, G.; David Raju, B.; Rama Rao, K.S. Vapor phase esterification of levulinic acid over ZrO_2/SBA-15 catalyst. *Catal. Commun.* **2016**, *75*, 1−5.

(66) Dharne, S.; Bokade, V. V. Esterification of levulinic acid to n-butyl levulinate over heteropolyacid supported on acid-treated clay. *Journal of Natural Gas Chemistry* **2011**, *20*, 18−24.

(67) Pasquale, G.; Vazquez, P.; Romanelli, G.; Baronetti, G. Catalytic upgrading of levulinic acid to ethyl levulinate using reusable silica-included Wells-Dawson heteropolyacid as catalyst. *Catal. Commun.* **2012**, *18*, 115−120.

(68) Yan, K.; Wu, G.; Wen, J.; Chen, A. One-step synthesis of mesoporous $H_4SiW_{12}O_{40}$-SiO_2 catalysts for the production of methyl and ethyl levulinate biodiesel. *Catal. Commun.* **2013**, *34*, 58−63.

(69) Yadav, G. D.; Yadav, A. R. Synthesis of ethyl levulinate as fuel additives using heterogeneous solid superacidic catalysts: Efficacy and kinetic modeling. *Chemical Engineering Journal* **2014**, *243*, 556−563.

(70) Kuwahara, Y.; Kaburagi, W.; Nemoto, K.; Fujitani, T. Esterification of levulinic acidwith ethanol over sulfated Si-doped ZrO_2 solid acid catalyst: Study of the structure- activity relationships. *Applied Catalysis A: General* **2014**, *476*, 186−196.

(71) Su, F.; Ma, L.; Song, D.; Zhang, X.; Guo, Y. Design of a highly ordered mesoporous $H_3PW_{12}O_{40}/ZrO_2$-Si(Ph)Si hybrid catalyst for methyl levulinate synthesis. *Green Chem.* **2013**, *15*, 885−890.

(72) Su, F.; An, S.; Song, D.; Zhang, X.; Lu, B.; Guo, Y. Heteropoly acid and ZrO_2 bifunctionalized organosilica hollow nanospheres for esterification and transesterification. *Journal of Materials Chemistry A* **2014**, *2*, 14127−14138.

(73) Song, D.; An, S.; Sun, Y.; Guo, Y. Efficient conversion of levulinic acid or furfuryl alcohol into alkyl levulinates catalyzed by heteropoly acid and ZrO_2 bifunctionalized organosilica nanotubes. *J. Catal.* **2016**, *333*, 184−199.

(74) Pileidis, F. D.; Tabassum, M.; Coutts, S.; Titirici, M.-M. Esterification of levulinic acid into ethyl levulinate catalysed by sulfonated hydrothermal carbons. *Chinese Journal of Catalysis* **2014**, *35*, 929−936.

(75) Barrett, E. P.; Joyner, L. G.; Halenda, P. P. The determination of pore volume and area distributions in porous substances. I. Computations from nitrogen isotherms. *J. Am. Chem. Soc.* **1951**, *73*, 373−380.

(76) Lin, K. L.; Wang, H. C. Hydrolysis of zirconium alkoxide under an uncontrolled atmosphere. *J. Mater. Sci.* **1988**, *23*, 3666−3670.

(77) Casula, M. F.; Loche, D.; Marras, S.; Paschina, G.; Corrias, A. Role of urea in the preparation of highly porous nanocomposite aerogels. *Langmuir* **2007**, *23*, 3509−3512.

(78) Klicova, L.; Sebej, P.; Stacko, P.; Filippov, S. K.; Bogomolova, A.; Padilla, M.; Klan, P. CTAB/water/chloroform reverse micelles: a closed or open association model? *Langmuir* **2012**, *28*, 15185−15192.

(79) Porter, D. L.; Heuer, A. H. Microstructural Development in MgO-Partially Stabilized Zirconia (Mg-PSZ). *Journal of the American Ceramic Society* **1979**, *62*, 298−305.

(80) Li, M.; Feng, Z.; Xiong, G.; Ying, P.; Xin, Q.; Li, C. Phase transformation in the surface region of zirconia detected by UV Raman spectroscopy. *J. Phys. Chem. B* **2001**, *105*, 8107−8111.

(81) Joo, J.; Yu, T.; Kim, Y. W.; Park, H. M.; Wu, F.; Zhang, J. Z.; Hyeon, T. Multigram scale synthesis and characterization of monodisperse tetragonal zirconia nanocrystals. *J. Am. Chem. Soc.* **2003**, *125*, 6553−6557.

(82) Masika, E.; Mokaya, R. Hydrogen storage in high surface area carbons with identical surface areas but different pore sizes: direct demonstration of the effects of pore size. *J. Phys. Chem. C* **2012**, *116*, 25734−25740.

(83) El-Safty, S. A.; Mizukami, F.; Hanaoka, T. General and simple approach for control cage and cylindrical mesopores, and thermal/hydrothermal sTable frameworks. *J. Phys. Chem. B* **2005**, *109*, 9255−9264.

(84) Wang, W.-K.; Zheng, M.-L.; Chen, W.-Q.; Jin, F.; Cao, Y.-Y.; Zhao, Z.-S.; Duan, X.-M. Microscale golden candock leaves self-aggregated on a polymer surface: Raman scattering enhancement and Superhydrophobicity. *Langmuir* **2011**, *27*, 3249−3253.

(85) de Boer, J.H.; Lippens, B.C.; Linsen, B.G.; Broekhoff, J.C.P.; van den Heuvel, A.; Osinga, T. J. Thet-curve of multimolecular N 2-adsorption. *J. Colloid Interface Sci.* **1966**, *21*, 405−414.

(86) Sing, K. S. W. Reporting physisorption data for gas/solid systems with special reference to the determination of surface area and porosity (Recommendations 1984). *Pure Appl. Chem.* **1985**, *57*, 603−619.

(87) Antonelli, D. M.; Ying, J. Y. Synthesis of a STable Hexagonally Packed Mesoporous Niobium Oxide Molecular Sieve Through a Novel Ligand-Assisted Templating Mechanism. *Angew. Chem., Int. Ed. Engl.* **1996**, *35*, 426−430.

(88) Yang, P.; Zhao, D.; Margolese, D. I.; Chmelka, B. F.; Stucky, G. D. Generalized syntheses of large-pore mesoporous metal oxides with semicrystalline frameworks. *Nature* **1998**, *396*, 152−155.

(89) Armelao, L.; Tondello, E.; Bigliani, L.; Bottaro, G. ZrO_2 Sol-Gel Thin Films by XPS. *Surf. Sci. Spectra* **2001**, *8*, 268−273.

(90) Barreca, D.; Battiston, G. A.; Gerbasi, R.; Tondello, E.; Zanella, P. Zirconium dioxide thin films characterized by XPS. *Surf. Sci. Spectra* **2000**, *7*, 303−309.

(91) Patel, K. J.; Desai, M. S.; Panchal, C. J. The influence of substrate temperature on the structure, morphology, and optical properties of ZrO_2 thin films prepared by e-beam evaporation. *Adv. Mater. Lett.* **2012**, *3*, 410−414.